MAGNETISM

Probing magnetism in 2D van der Waals crystalline insulators via electron tunneling

D. R. Klein[1]*, D. MacNeill[1]*, J. L. Lado[2,3], D. Soriano[2], E. Navarro-Moratalla[4], K. Watanabe[5], T. Taniguchi[5], S. Manni[6,7,8], P. Canfield[6,7], J. Fernández-Rossier[2], P. Jarillo-Herrero[1]†

Magnetic insulators are a key resource for next-generation spintronic and topological devices. The family of layered metal halides promises varied magnetic states, including ultrathin insulating multiferroics, spin liquids, and ferromagnets, but device-oriented characterization methods are needed to unlock their potential. Here, we report tunneling through the layered magnetic insulator CrI_3 as a function of temperature and applied magnetic field. We electrically detect the magnetic ground state and interlayer coupling and observe a field-induced metamagnetic transition. The metamagnetic transition results in magnetoresistances of 95, 300, and 550% for bilayer, trilayer, and tetralayer CrI_3 barriers, respectively. We further measure inelastic tunneling spectra for our junctions, unveiling a rich spectrum consistent with collective magnetic excitations (magnons) in CrI_3.

Van der Waals magnetic insulators are a materials system that may enable designer topological states (*1*) and spintronic technologies (*2*). The recent isolation (*3*, *4*) of few-layer magnets with either ferromagnetic (CrI_3, $Cr_2Ge_2Te_6$) or antiferromagnetic order (*5*, *6*) is just the tip of the iceberg. The vast family of layered metal halides (*7*) contains spin orders from multiferroics (*8*) to proximate spin liquids (*9*), of key interest to both fundamental and applied physics. Existing studies have focused on magneto-optical effects (*3*, *4*, *10*, *11*) as a characterization tool, but a more general, device-oriented, approach is needed.

Here we demonstrate that tunneling through layered insulators is a versatile probe of magnetism on the nanoscale in these materials. We report the conductance of graphite/CrI_3/graphite junctions (Fig. 1A) as a function of magnetic field and temperature and electrically detect an antiferromagnetic ground state and a field-induced metamagnetic transition. The metamagnetic transition is revealed by large magnetoresistances (up to 550%) arising from the antiparallel-to-parallel reorientation of chromium spins in adjacent crystal layers. A similar effect was previously proposed (*12*) for synthetic multilayer magnets, but experimental realizations (*13*) were limited to magnetoresistances below 70%. The performance of our devices is an order of magnitude higher, corresponding to estimated spin polarization above 95%. Furthermore, the two-dimensional magnetism of CrI_3 enables ultrathin tunnel barriers (<3 nm) and a concomitant 10,000-fold increase in conductance (per unit area) compared to previous results (*13*). The noninvasive van der Waals transfer of the magnetic layer ensures substrate-independent device integration, and together with high magnetoresistance, spin polarization, and conductance, may enable noninvasive spin injectors and detectors for next-generation spintronics experiments incorporating topological insulators (*14*), superconductors (*15*), antiferromagnets (*16*), and low-symmetry crystals (*17*–*20*).

Tunneling through magnetic insulators was first studied in the pioneering experiments of (*21*) and later in (*22*, *23*). When electrons tunnel through a ferromagnetic insulator, spin-up and spin-down electrons see different barrier heights (Fig. 1B). As a result, the tunneling rate can vary by orders of magnitude for electrons of opposite spins (*12*, *22*), called the spin filter effect. The smaller gap for spin-up electrons tends to decrease the junction resistance as the barrier is cooled below its Curie temperature, T_C. The situation is more complicated for spatially textured magnetism. For example, the resistance of Ag/EuSe/Al tunnel junctions increases significantly when the EuSe becomes antiferromagnetic (*23*). However, the exponential dependence of the tunneling current on the barrier electronic structure generally provides a clear resistive signature of magnetism. We will use these effects to electrically detect the magnetic ground state and field-induced metamagnetic transition of few-layer CrI_3.

The resistance of a graphite/tetralayer CrI_3/graphite junction (device D1) as a function of temperature is shown in Fig. 1C. We measure the resistance in a four-point geometry using a 30-mV root-mean-square AC excitation (*24*). The temperature dependence was measured by cooling the sample down with (purple line) and without (black line) the application of an external magnetic field. The magnetic field is applied perpendicular to the layers, along the magnetic easy axis of CrI_3. Above 90 K, the resistance is independent of the applied field and shows Arrhenius behavior with a thermal activation gap of roughly 159 meV (fig. S1). The resistance becomes field-dependent as the temperature approaches the bulk T_C of 61 K. When the sample is cooled in a 2.5-T magnetic field, the resistance plateaus below 80 K, signaling the onset of tunneling conductance (*21*, *23*). By contrast, when the sample is cooled without an external field, the resistance exhibits a kink near T_C and continues to increase below 60 K. The dependence of the tunneling resistance on magnetic field and temperature shows that the tunnel conductance is sensitive to the magnetization of the barrier.

To further investigate the magnetic phase diagram, we study the zero-bias conductance (500-μV AC excitation) of devices with two- to four-layer CrI_3 barriers as a function of applied magnetic field at low temperatures (300 mK to 4.2 K). We start with an analysis of a graphite/bilayer CrI_3/graphite junction (D2, Fig. 2A). For this device, the junction conductance increases almost twofold in a sharp step as the external field is increased above 0.85 T. The corresponding magnetoresistance is 95%, defined as

$$MR = 100\% \times \frac{(G_{HI} - G_{LO})}{G_{LO}} \quad (1)$$

where G_{HI} is the high-field conductance maximum and G_{LO} is the low-field conductance minimum. No further steps are observed up to the largest fields studied (8 T; see fig. S2). As the field is reduced from 2.4 T, the conductance decreases to its original zero-field value in a sharp step at 0.35 T. The well-defined steps and hysteretic field dependence demonstrate that the conductance changes originate from switching events of the magnetization. The tunneling current is most sensitive to the interlayer magnetization alignment, so the large steps we observe likely arise from vertical domains, i.e., regions where the magnetization points in different directions in different layers of CrI_3.

Recently, magneto-optical Kerr effect (MOKE) data have revealed an antiferromagnetic state in bilayer CrI_3 for fields below about 0.6 T (*4*). In this state, the Cr moments order ferromagnetically within each layer but point in opposite directions in adjacent layers (Fig. 2B). The layers are fully aligned when the external magnetic field is increased above a critical value (Fig. 2C); i.e., it undergoes a metamagnetic transition to a ferromagnetic state. When the field is reduced, the magnetization spontaneously reverts to the antiparallel configuration. The switching behavior we observe in magnetoconductance reflects these previous MOKE data, confirming that the conductance change arises from the metamagnetic

[1]Department of Physics, Massachusetts Institute of Technology, Cambridge, MA 02139, USA. [2]QuantaLab, International Iberian Nanotechnology Laboratory, 4715-310 Braga, Portugal. [3]Institute for Theoretical Physics, ETH Zurich, 8093 Zurich, Switzerland. [4]Instituto de Ciencia Molecular, Universidad de Valencia, 46980 Paterna, Spain. [5]National Institute for Materials Science, Tsukuba, Japan. [6]Ames Laboratory, U.S. Department of Energy, Iowa State University, Ames, IA 50011, USA. [7]Department of Physics and Astronomy, Iowa State University, Ames, IA 50011, USA. [8]Department of Condensed Matter Physics and Materials Science, Tata Institute of Fundamental Research, Mumbai 400005, India.
*These authors contributed equally to this work.
†Corresponding author. Email: pjarillo@mit.edu

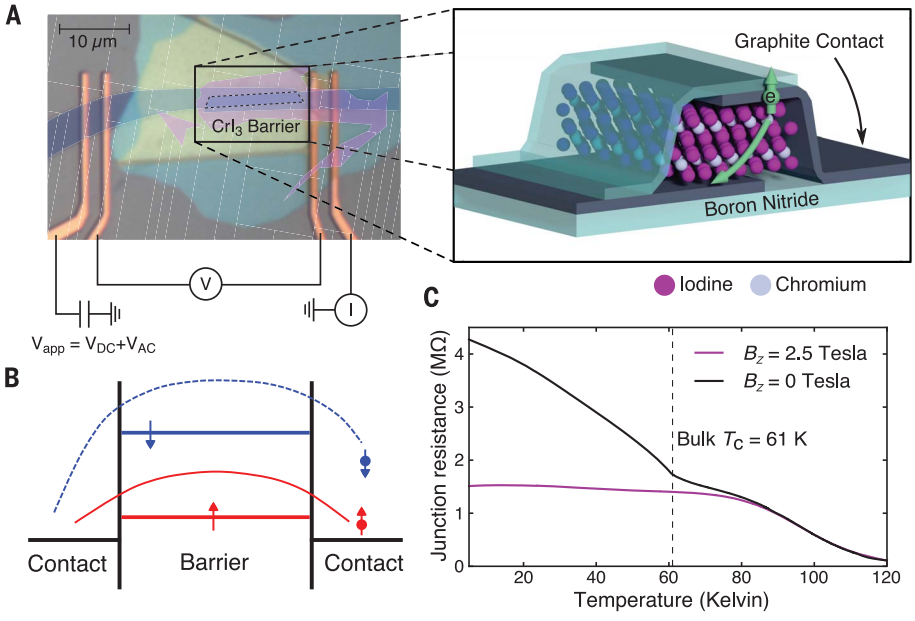

Fig. 1. Experimental setup. (**A**) Optical micrograph of a tetralayer CrI_3 tunnel junction device (device D1, false color). The dashed line encloses the tunnel junction area. The graphite contacts are themselves contacted by Au/Cr wires in a four-point geometry. Inset: Schematic of the van der Waals heterostructures studied in this work. Electrons tunnel between two graphite sheets separated by a magnetic CrI_3 tunnel barrier. The entire stack is encapsulated in hexagonal boron nitride. (**B**) Schematic energy diagram of a metal/ferromagnetic insulator/metal junction. The red and blue lines in the barrier region represent the spin-up and spin-down energy barriers, respectively. The lower barrier for spin-up electrons leads to spin-polarized tunneling and reduced resistance for a ferromagnetic barrier. (**C**) Zero-bias junction resistance versus temperature for device D1 cooled with (purple) and without (black) an applied magnetic field. The curves begin to deviate around the bulk Curie temperature (61 K), giving evidence for magnetic order in the CrI_3 barrier and for spin-polarized tunneling. The magnetic field was applied perpendicular to the CrI_3 layers.

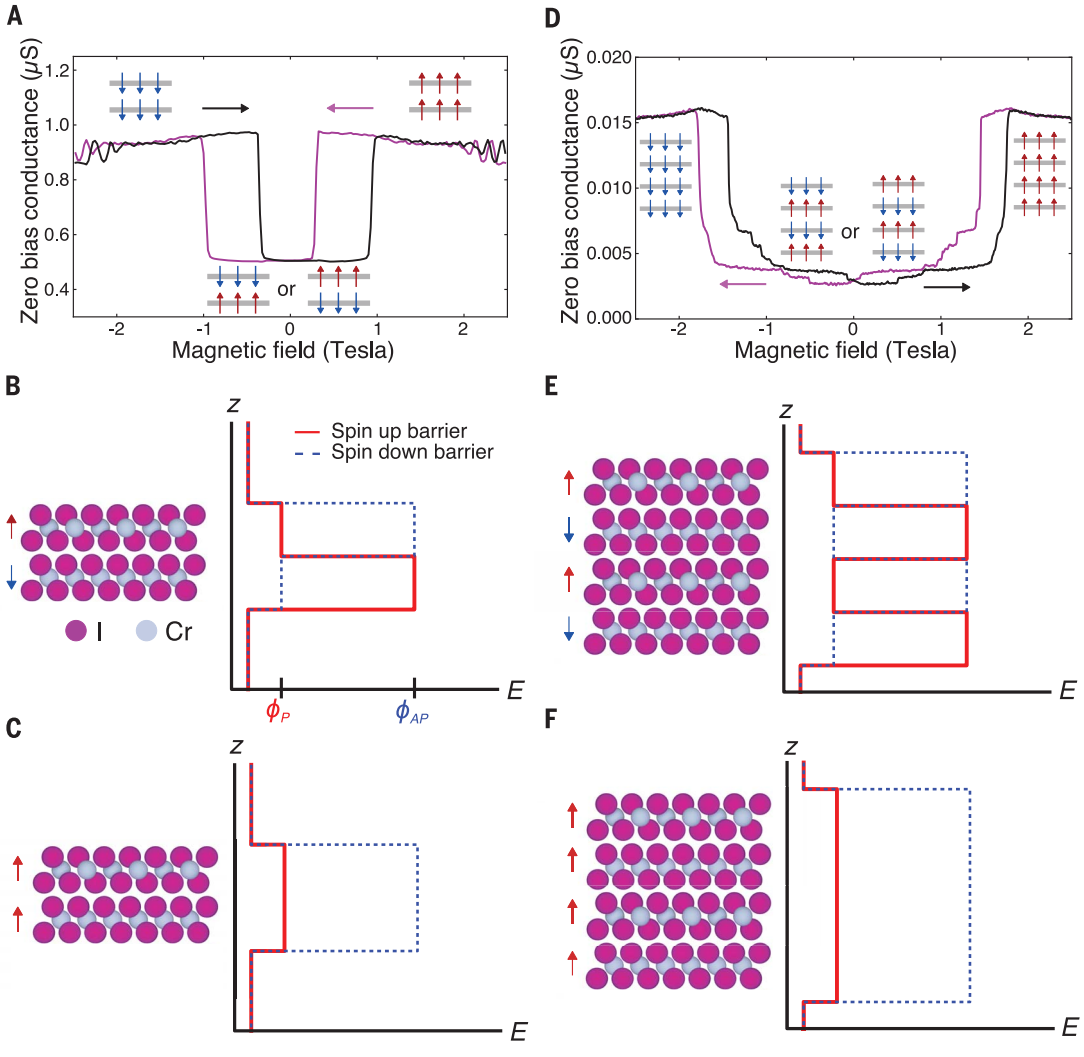

Fig. 2. Magnetoconductance of few-layer CrI_3. (**A**) Conductance through a bilayer CrI_3 tunnel barrier (device D2) as a function of an out-of-plane applied magnetic field with 500-μV AC excitation. The data were taken both for decreasing (purple line, left arrow) and increasing (black line, right arrow) magnetic field. The magnetoconductance traces are consistent with previous magnetometry data (*4*) for bilayer CrI_3 showing that the two layers are antiparallel at zero field but can be aligned with an external field below 1 T. (**B** and **C**) Schematic of barriers experienced by spin-up and spin-down electrons tunneling through bilayer CrI_3 in the low-field (B) and high-field (C) states. In the low-field state, the two layers are antiparallel, and both spins see a high barrier. In the high-field state, the layers are aligned and up spins see a low-energy barrier, leading to increased conductance. (**D** to **F**) Analogous data and schematics for a tetralayer CrI_3 barrier device (device D3). In both cases, the sample temperature was 300 mK.

transition. We note, however, that little to no hysteresis was previously observed in the MOKE results for bilayer CrI_3 (*4*), whereas we observe a clear hysteresis in the tunneling measurements. The reasons for this may be related to the lower temperature for these tunneling experiments as well as the fact that the CrI_3 remains closer to equilibrium (no photoexcitation).

We have also studied tunnel junctions with three- and four-layer CrI_3 as the barrier. The zero-bias junction resistance of a graphite/4L CrI_3/graphite junction (D3) is shown as a function of external magnetic field in Fig. 2D. The overall phenomenology is similar to that of junctions with a bilayer barrier, with well-defined steps and a total magnetoresistance of 550%. In addition to the large jump around 1.8 T, we see multiple smaller steps that may correspond to lateral domains within the junction. This is consistent with a lateral domain size on the order of 2 μm observed in previous optical studies (*2*, *4*). The behavior of our trilayer junctions is again similar, with magnetoresistances up to 300% (fig. S3). On the basis of these results, we hypothesize that few-layer CrI_3 is antiferromagnetic without an external magnetic field (Fig. 2E). Such behavior is consistent with magneto-optical data for bilayer CrI_3 (*4*), but those MOKE data suggested a ferromagnetic configuration for thicker crystals (e.g., 3L CrI_3). Nevertheless, our data strongly support an antiparallel alignment between layers extending over most of the junction area. Once more, the different temperatures and absence of photoexcitation may be responsible for the different behavior observed.

To understand the large magnetoresistance and its thickness dependence, we analyze a spin filter model (*12*) for transmission through a CrI_3 barrier. The model treats each crystal layer of the CrI_3 as an independent tunnel barrier, with a transmission coefficient of T_P and T_{AP} for spins parallel and antiparallel to the local spin direction, respectively. Ignoring multiple reflections and quantum interference effects, the transmission through the entire crystal is then a product of the transmission coefficients for each layer. For example, for a CrI_3 bilayer in the high-field magnetization configuration (Fig. 2C), spin-up electrons have a transmission probability T_P^2 whereas spin-down electrons have transition probability T_{AP}^2. The high-field conductance is $G_{HI} \propto T_P^2 + T_{AP}^2$. Similarly, for the low-field configuration with antiparallel magnetizations (Fig. 2B), the conductance is $G_{LO} \propto 2T_PT_{AP}$. The ratio of high-field to low-field conductances is then $G_{HI}/G_{LO} = (T_P^2 + T_{AP}^2)/2T_PT_{AP} \approx T_P/2T_{AP}$. We have carried out similar calculations for N = 3- and 4-layer CrI_3 barriers, summarized in the supplementary text. In Fig. 3A, we plot the measured magnetoresistance (black circles) as a function of N, along with a one-parameter fit to the spin filter model (purple stars). The model reproduces the overall experimental trend with a best-fit value of T_P/T_{AP} = 3.5. For a summary of all measured devices, see table S1.

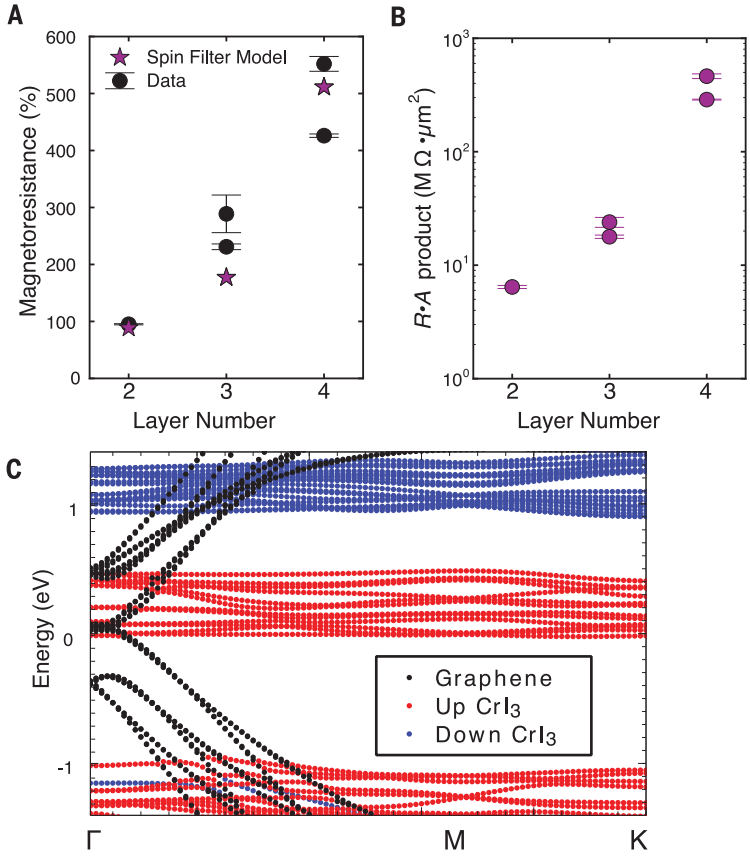

Fig. 3. Origin of magnetoresistance in CrI_3. (**A**) Magnetoresistance ratio (black circles) versus CrI_3 layer number for multiple devices at 300 mK. We also plot a fit to the spin filter model (purple stars). The only fitting parameter, T_P/T_{AP} = 3.5, gives the ratio of spin-up to spin-down transmission through a CrI_3 monolayer. (**B**) Resistance-area product versus CrI_3 layer number for multiple devices. The resistances are measured in the fully aligned magnetic configuration and were taken at zero bias. (**C**) Electronic structure of a trilayer graphite/trilayer CrI_3 heterostructure calculated with density functional theory. The CrI_3 is in the fully ferromagnetic configuration, and its bands are projected on the spin-up and spin-down channels. Although the minority spins do not show states close to the Fermi energy, there are a large number of states in the majority channel. The difference establishes a microscopic basis for the large T_P/T_{AP} that we observe.

We can also estimate the spin polarization of the current within the spin filter model. When the CrI_3 is fully polarized, the transmission probability of up and down spins through an N-layer CrI_3 barrier is T_P^N and T_{AP}^N, respectively. Therefore, the ratio of spin-up to spin-down conductance is approximately $G_\uparrow/G_\downarrow = (T_P/T_{AP})^N$. From $T_P/T_{AP} \approx 3.5$, we estimate a spin polarization of $(G_\uparrow - G_\downarrow)/(G_\uparrow + G_\downarrow) \approx 85$, 95, and 99% for N = 2, 3, and 4, respectively. These values are comparable to the largest values obtained with EuSe and EuS magnetic insulator barriers (*13*, *23*), so that CrI_3 tunnel barriers can enable future spin-sensitive transport devices.

In the spin filter approximation, the calculation of the magnetoresistance is reduced to a calculation of T_P/T_{AP}, related to the different barrier heights for spin-up and spin-down electrons. To investigate the barrier heights, we carried out density functional theory (DFT) calculations for three layers of CrI_3 and three layers of graphite (see the supplementary text). Calculations portray CrI_3 as a ferromagnetic insulator with magnetic moments localized on the chromium atoms and spin-split energy bands (Fig. 3C). Notably, when the magnetization of the three layers is aligned, we find that spin-up bands of CrI_3 lie very close to the graphite Fermi energy, whereas the nearest spin-down bands are much higher in energy (>1 eV). Therefore, the transparency of the barrier has to be much smaller for spin-down electrons and provides a microscopic foundation for the large T_P/T_{AP}. Note that even though the DFT calculations show a CrI_3 majority band very close to or crossing the graphite Fermi energy, the exponential thickness dependence of the junction resistance (Fig. 3B) shows that our junctions are in the tunneling-dominated regime with a finite barrier height. Further transport calculations should elucidate the precise tunneling pathways in CrI_3/graphite junctions leading to finite energy barriers with chromium 3d orbital bands very close to the Fermi level.

In addition to the zero-bias conductance, we measured the differential conductance dI/dV as a function of the applied DC offset V_{DC}. The

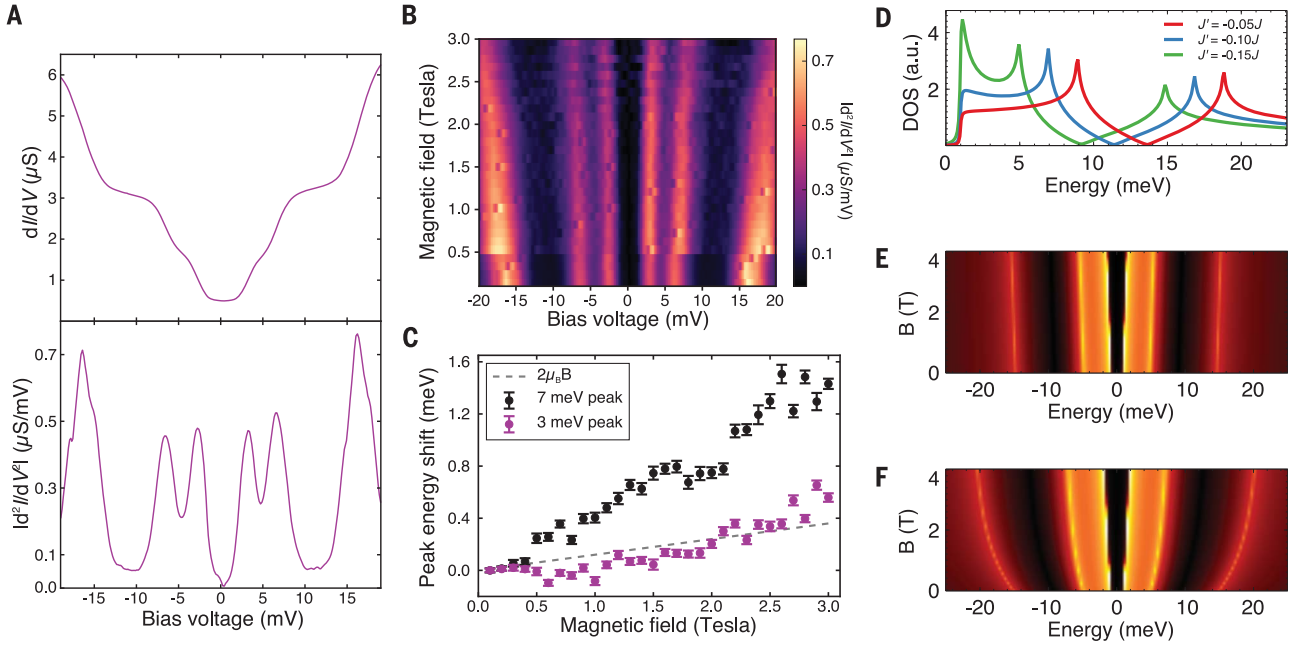

Fig. 4. Inelastic tunneling spectroscopy. (**A**) Top panel: Differential conductance versus a DC bias voltage for a bilayer CrI_3 barrier device (D2) at zero applied magnetic field. The AC excitation was 200 μV and the temperature was 300 mK. Bottom panel: Absolute value of d^2I/dV^2 versus a DC bias voltage, obtained via numerical differentiation of the data in the top panel. According to the theory of inelastic tunneling spectroscopy, the peaks in d^2I/dV^2 correspond to phonon or magnon excitations of the barrier or electrodes. (**B**) $|d^2I/dV^2|$ (color scale at right) versus applied magnetic field and DC bias voltage. All three inelastic peaks increase in energy as the applied field is increased. (**C**) Energy of the two lowest-energy inelastic peaks versus applied magnetic field. The zero-field energy is subtracted from both peaks for clarity. The peak locations were determined by Gaussian fits to the data. The error bars represent estimated standard deviations calculated from the least-squares fitting procedure. The dashed gray line shows the Zeeman energy shift of a $2\mu_B$ magnetic moment (0.12 meV/T), which roughly matches the evolution of the 3-meV peak. (**D**) Calculated magnon density of states (DOS) for CrI_3. The details of the calculations are described in the supplementary text. (**E**) Calculated dispersion of magnons with applied magnetic field at zero temperature. (**F**) Calculated renormalized magnon dispersion with magnetic field at finite temperature ($T = 0.033J$, where J is the nearest-neighbor exchange).

dI/dV versus V_{DC} traces reveal a rich spectrum, whose most prominent features are a series of steplike increases, symmetric in bias, below 25 meV (Fig. 4 and figs. S4 and S5). These steps are characteristic of inelastic electron tunneling where electrons lose energy to collective excitations of the barrier or electrodes. When the tunneling energy (eV_{DC}) exceeds the collective excitation energy, the introduction of these additional tunneling pathways results in steps in the dI/dV versus V_{DC} trace. The energies of phonons (*25*–*27*) and magnons (*28*–*31*) can therefore be measured as peaks (dips) in d^2I/dV^2 versus V_{DC} for positive (negative) V_{DC}. The bottom panel of Fig. 4A shows $|d^2I/dV^2|$ obtained by numerical differentiation of the dI/dV data for a bilayer CrI_3 barrier device (D2). The inelastic tunneling spectrum (IETS) reveals three peaks at 3, 7 , and 17 meV. These features were visible in every CrI_3 tunneling device that we measured (figs. S4 to S6). Past IETS data on graphite/boron nitride/graphite heterostructures in a geometry similar to that of our junctions (*26*) do not contain any inelastic contributions from graphite phonons below 17 meV. Earlier scanning tunneling studies of graphite surfaces similarly find an onset of prominent graphite inelastic peaks at 16 meV (*27*). Thus, the inner two peaks must arise from CrI_3 phonons or magnons. The inelastic features start forming just below the onset of magnetism (fig. S7), suggesting a magnon excitation origin.

Another signature of magnon-assisted tunneling is the stiffening of the magnon modes as an external magnetic field is applied (*29*, *30*). A single magnon corresponds to a delocalized spin-flip ($|S_z| = 1$) within the CrI_3 barrier, which carries a magnetic moment of approximately $2\mu_B$ (where μ_B is the Bohr magneton) antiparallel to the external magnetic field. Therefore, magnon IETS peaks should blueshift at 0.12 meV/T by the Zeeman effect. Figure 4B shows $|d^2I/dV^2|$ as a function of both applied magnetic field and bias voltage. Even to the eye, a strong linear increase of all three IETS peaks is visible. In Fig. 4C, we plot the peak energies (determined by Gaussian fits) of the innermost peaks versus magnetic field. We also plot the expected energy shift $2\mu_B B$ due to the Zeeman effect (dashed gray line). This line roughly fits the magnetic field dependence of the 3-meV peak, but the 7-meV peak clearly has much higher dispersion corresponding to $8\mu_B$. The latter effect might be caused by magnon renormalization effects, as discussed below.

To model the magnon spectrum, we write an effective spin Hamiltonian for CrI_3 (*32*) that includes nearest- and next-nearest–neighbor exchange, together with an easy axis anisotropy term (see supplementary text for details). Using this model, we find that the calculated magnon density of states (Fig. 4D) can qualitatively reproduce the experimental inelastic spectrum. We used a nearest-neighbor exchange parameter consistent with previous first principles calculations and experiment (*32*–*34*) and chose the next-nearest–neighbor value to match our data (see supplementary text). At zero temperature, the magnon energies are still expected to blueshift at 0.12 meV/T in an applied magnetic field (Fig. 4E). However, at finite temperature and $B = 0$, thermally excited magnons deplete the magnetization, resulting in an effective reduction of the spin stiffness and a redshift of the magnon spectrum with respect to the case without thermal renormalization of the exchange constants. Application of a magnetic field increases the spin wave gap, decreasing the population of thermal spin waves and increasing the spin stiffness. This renormalizes the effective magnon hopping parameters, leading to a shift of the spin wave spectrum that adds to the Zeeman term and results in a nonlinear field dependence (Fig. 4F and supplementary text).

Our devices are an example of a "double spin filter" where a magnetic tunnel barrier with decoupled magnetic layers is used as a magnetic

memory bit (*12*). We overcome the limitations of previous double spin filters (*13*) owing to the unique decoupling of magnetic layers across the atomic-scale van der Waals gap. This decoupling provides electrical readout of the CrI_3 magnetization state without additional ferromagnetic sensor layers, enabling facile detection of spin-orbit torques on layered magnetic insulators. Further exploration is required to understand the electron-magnon coupling in these devices and to potentially study bosonic topological matter in honeycomb ferromagnets (*35*, *36*).

REFERENCES AND NOTES

1. W.-K. Tse, Z. Qiao, Y. Yao, A. H. MacDonald, Q. Niu, *Phys. Rev. B* **83**, 155447 (2011).
2. D. Zhong *et al*., *Sci. Adv.* **3**, e1603113 (2017).
3. M. A. McGuire, H. Dixit, V. R. Cooper, B. C. Sales, *Chem. Mater.* **27**, 612–620 (2015).
4. B. Huang *et al*., *Nature* **546**, 270–273 (2017).
5. X. Wang *et al*., *2D Mater.* **3**, 031009 (2016).
6. J.-U. Lee *et al*., *Nano Lett.* **16**, 7433–7438 (2016).
7. M. A. McGuire, *Crystals (Basel)* **7**, 121 (2017).
8. T. Kurumaji *et al*., *Phys. Rev. Lett.* **106**, 167206 (2011).
9. A. Banerjee *et al*., *Science* **356**, 1055–1059 (2017).
10. C. Gong *et al*., *Nature* **546**, 265–269 (2017).
11. K. L. Seyler *et al*., *Nat. Phys.* **14**, 277–281 (2018).
12. D. C. Worledge, T. H. Geballe, *J. Appl. Phys.* **88**, 5277–5279 (2000).
13. G.-X. Miao, M. Müller, J. S. Moodera, *Phys. Rev. Lett.* **102**, 076601 (2009).
14. A. R. Mellnik *et al*., *Nature* **511**, 449–451 (2014).
15. T. Wakamura *et al*., *Nat. Mater.* **14**, 675–678 (2015).
16. P. Wadley *et al*., *Science* **351**, 587–590 (2016).
17. D. MacNeill *et al*., *Nat. Phys.* **13**, 300–305 (2017).
18. D. MacNeill *et al*., *Phys. Rev. B* **96**, 054450 (2017).
19. Q. Shao *et al*., *Nano Lett.* **16**, 7514–7520 (2016).
20. T. D. Skinner *et al*., *Nat. Commun.* **6**, 6730 (2015).
21. L. Esaki, P. J. Stiles, S. von Molnar, *Phys. Rev. Lett.* **19**, 852–854 (1967).
22. J. S. Moodera, X. Hao, G. A. Gibson, R. Meservey, *Phys. Rev. Lett.* **61**, 637–640 (1988).
23. J. S. Moodera, R. Meservey, X. Hao, *Phys. Rev. Lett.* **70**, 853–856 (1993).
24. Materials and methods are available as supplementary materials.
25. R. C. Jaklevic, J. Lambe, *Phys. Rev. Lett.* **17**, 1139–1140 (1966).
26. S. Jung *et al*., *Sci. Rep.* **5**, 16642 (2015).
27. L. Vitali, M. A. Schneider, K. Kern, L. Wirtz, A. Rubio, *Phys. Rev. B* **69**, 121414 (2004).
28. D. C. Tsui, R. E. Dietz, L. R. Walker, *Phys. Rev. Lett.* **27**, 1729–1732 (1971).
29. C. F. Hirjibehedin, C. P. Lutz, A. J. Heinrich, *Science* **312**, 1021–1024 (2006).
30. A. Spinelli, B. Bryant, F. Delgado, J. Fernández-Rossier, A. F. Otte, *Nat. Mater.* **13**, 782–785 (2014).
31. K. Yamaguchi, *Phys. Status Solidi, B Basic Res.* **236**, 634–639 (2003).
32. J. L. Lado, J. Fernández-Rossier, *2D Mater.* **4**, 035002 (2017).
33. W.-B. Zhang, Q. Qu, P. Zhu, C.-H. Lam, *J. Mater. Chem. C Mater. Opt. Electron. Devices* **3**, 12457–12468 (2015).
34. A. Narath, *Phys. Rev.* **140**, A854–A862 (1965).
35. S. A. Owerre, *Sci. Rep.* **7**, 6931 (2017).
36. S. S. Pershoguba *et al*., *Phys. Rev. X* **8**, 011010 (2018).
37. D. Klein, Replication Data for: Probing magnetism in 2D van der Waals crystalline insulators via electron tunneling, Version 1, Harvard Dataverse (2018); https://doi.org/10.7910/DVN/4RUPNW.

ACKNOWLEDGMENTS

We thank V. Fatemi and Y. Cao for helpful discussions and assistance with measurements. **Funding:** This work was supported by the Center for Integrated Quantum Materials under NSF grant DMR-1231319 as well as the Gordon and Betty Moore Foundation's EPiQS Initiative through grant GBMF4541 to P.J.-H. Device fabrication was partly supported by the Center for Excitonics, an Energy Frontier Research Center funded by the U.S. Department of Energy (DOE), Office of Basic Energy Sciences (BES), under award no. DESC0001088. D.R.K. acknowledges partial support by the NSF Graduate Research Fellowship Program under grant no. 1122374. J.L.L. acknowledges financial support from the ETH Zurich Postdoctoral Fellowship program. D.S. acknowledges the Marie Curie Cofund program at INL. J.F.-R. acknowledges support from PTDC/FIS-NAN/3668/2014. Growth of hexagonal boron nitride crystals at NIMS was supported by the Elemental Strategy Initiative conducted by the MEXT, Japan, and JSPS KAKENHI grant nos. JP15K21722 and JP25106006. Work done at Ames Laboratory (P.C. and S.M.) was supported by the DOE BES Division of Materials Sciences and Engineering. Ames Laboratory is operated for the DOE by Iowa State University under contract no. DE-AC02-07CH11358. S.M. was funded by the Gordon and Betty Moore Foundation's EPiQS Initiative through grant GBMF4411. **Author contributions:** D.R.K., D.M., and P.J.-H. conceived the project. D.R.K. and D.M. fabricated and measured devices and analyzed the data. K.W., T.T., S.M., and P.C. supplied the boron nitride crystals. E.N.-M. supplied the CrI_3 crystals. J.L.L., D.S., and J.F.-R. carried out theoretical calculations. All authors contributed to writing the manuscript. **Competing interests:** The authors declare no competing financial interests. **Data and materials availability:** The data shown in the paper are available at Harvard Dataverse (*37*).

SUPPLEMENTARY MATERIALS

www.sciencemag.org/content/360/6394/1218/suppl/DC1
Materials and Methods
Supplementary Text
Figs. S1 to S8
Table S1
References (*38*–*41*)

21 November 2017; accepted 24 April 2018
Published online 3 May 2018
10.1126/science.aar3617

Science

Probing magnetism in 2D van der Waals crystalline insulators via electron tunneling

D. R. Klein, D. MacNeill, J. L. Lado, D. Soriano, E. Navarro-Moratalla, K. Watanabe, T. Taniguchi, S. Manni, P. Canfield, J. Fernández-Rossier and P. Jarillo-Herrero

Science **360** (6394), 1218-1222.
DOI: 10.1126/science.aar3617originally published online May 3, 2018

An intrinsic magnetic tunnel junction

An electrical current running through two stacked magnetic layers is larger if their magnetizations point in the same direction than if they point in opposite directions. These so-called magnetic tunnel junctions, used in electronics, must be carefully engineered. Two groups now show that high magnetoresistance intrinsically occurs in samples of the layered material CrI_3 sandwiched between graphite contacts. By varying the number of layers in the samples, Klein *et al.* and Song *et al.* found that the electrical current running perpendicular to the layers was largest in high magnetic fields and smallest near zero field. This observation is consistent with adjacent layers naturally having opposite magnetizations, which align parallel to each other in high magnetic fields.

Science, this issue p. 1218, p. 1214

Science (print ISSN 0036-8075; online ISSN 1095-9203) is published by the American Association for the Advancement of Science, 1200 New York Avenue NW, Washington, DC 20005. The title *Science* is a registered trademark of AAAS.